Article

Molecularly Imprinted Polymer-Based Nanoporous Carbon Nanocomposite for Effective Adsorption of Hg(II) Ions from Aqueous Suspensions

Lawal Abubakar [1,2], **Nor Azah Yusof** [1,3,*], **Abdul Halim Abdullah** [1,3], **Faruq Mohammad** [4,*], **Mohd Hanif Wahid** [1], **Suhainie Ismail** [1,3], **Zulaiha Abdul Rahim** [1,3], **Hamad A. Al-Lohedan** [4] and **Ahmed A. Soleiman** [5]

1   Department of Chemistry, Faculty of Science, Universiti Putra Malaysia, Serdang 43400, Selangor, Malaysia; lawaligada@gmail.com (L.A.)
2   Department of Chemistry, Shehu Shagari College of Education Sokoto, Sokoto 840101, Sokoto State, Nigeria
3   Institute of Nanoscience and Nanotechnology (ION2), Universiti Putra Malaysia, Serdang 43400, Selangor, Malaysia
4   Department of Chemistry, College of Science, King Saud University, Riyadh 11451, Saudi Arabia
5   College of Sciences and Engineering, Southern University, Baton Rouge, LA 70813, USA
*   Correspondence: azahy@upm.edu.my (N.A.Y.); fmohammad@ksu.edu.sa (F.M.); Tel.: +966-11-467-5998 (F.M.)

Abstract: Due to the release of hazardous heavy metals from various industries, water pollution has become one of the biggest challenges for environmental scientists today. Mercury Hg(II) is regarded as one of the most toxic heavy metals due to its ability to cause cancer and other health issues. In this study, a tailor-made modern eco-friendly molecularly imprinted polymer (MIP)/nanoporous carbon (NC) nanocomposite was synthesized and examined for the uptake of Hg(II) using an aqueous solution. The fabrication of the MIP/NC nanocomposite occurred via bulk polymerization involving the complexation of the template, followed by polymerization and, finally, template removal. Thus, the formed nanocomposite underwent characterizations that included morphological, thermal degradation, functional, and surface area analyses. The MIP/NC nanocomposite, with a high specific surface area of 884.9 m^2/g, was evaluated for its efficacy towards the adsorptive elimination of Hg(II) against the pH solution changes, the dosage of adsorbent, initial concentration, and interaction time. The analysis showed that a maximum Hg(II) adsorption effectiveness of 116 mg/g was attained at pH 4, while the Freundlich model fitted the equilibrium sorption result and was aligned with pseudo-second-order kinetics. Likewise, thermodynamic parameters like enthalpy, entropy, and Gibbs free energy indicated that the adsorption was consistent with spontaneous, favorable, and endothermic reactions. Furthermore, the adsorption efficiency of MIP/NC was also evaluated against a real sample of condensate from the oil and gas industry, showing an 87.4% recovery of Hg(II). Finally, the synthesized MIP/NC showed promise as a selective adsorbent of Hg(II) in polluted environments, suggesting that a variety of combined absorbents of different precursors is recommended to evaluate heavy metal and pharmaceutical removals.

Keywords: molecularly imprinted polymer; nanoporous carbon; Hg(II) adsorption; thermodynamics; nanocomposite; palm-kernel shell

1. Introduction

Heavy metals are one of the world's most common environmental concerns because of their bioaccumulative and biomagnificent properties, which have rendered them unfriendly and extremely hazardous to aquatic and human life [1,2]. When there are certain quantities of heavy metals in water, sediment, air, and other environmental media exceeding the recommended limits, they cause a variety of diseases, such as memory loss, renal or kidney failure, lung damage, and reproductive system malfunctions [3]. Today, as a result of rapid urbanization and industrialization, heavy metal pollution constitutes a grave challenge

to the environment and to human life, particularly in emerging nations having polluted water bodies as a main source of drinking water for the populace [4]. Similarly, mercury, lead, zinc, arsenic, nickel, manganese, copper, cadmium, and chromium are toxic and potential carcinogens [5]. They are discharged into the environment, especially water sources, from natural and human-made sources, including dyes, fertilizers, pesticides, and other industrial products [6]. The World Health Organization (WHO) reported that the vast majority of the world's wastewater is being released into water bodies without any prior treatment because of social, economic, and political reasons. It is estimated that with the constant degradation of the natural environment and the unsustainable pressure being placed on worldwide water resources, by the year 2050, 45% of the universal GDP, 52% of the global population, and 40% of the world's grain manufacture will likely be affected [7].

According to the literature, mercury Hg(II) is one of the most toxic metal ions, causing acute and chronic toxicity to the central nervous system, kidneys, lung tissues, and reproductive system. This toxic metal ion can be found in the body of humans via intestinal ingestion, contact with skin, or blood circulation [8,9]. Hg(II) flows in the bloodstream (cells) and then accumulates in vital organs in the body, thereby causing paralysis, acute intestinal issues, and urinary and central nervous system disorders [10]. Mercury is ranked as the third most toxic ion by the Agency for Toxic Substances and Disease Registry (ATSDR) among the priority list of hazardous substances [11].

Due to continuous discharge from natural and industrial activities, Hg(II) contamination has become one of the environmental threats to the human populace and the entire world. Early research focused on Hg(II) removal using membrane processes, chemical precipitation, extraction, the exchange of ions, etc. [12]. Numerous papers have been published on the elimination of Hg(II) via various sources, namely molecularly imprinted polymers (MIPs) [13,14], graphene oxide [15,16], activated carbon [17–21], carbon nanotubes [22], biochar [23,24], magnetic materials [25], metals, and metal oxides [26]. Another water treatment technique that is commonly used for Hg(II) removal is adsorption, and this has become a more important technique due to its efficacy, ease, low cost, and practicality at low concentrations. In addition, the special advantages of employing this adsorption technique for Hg(II) adsorption include no sludge generation, high selectivity for Hg(II) against other heavy metals, and adaptability in adsorption media material selection. Therefore, applying agricultural biowaste as a solid adsorbent base serves as a simple, low-cost, eco-friendly treatment of Hg(II) from wastewater.

MIPs are highly selective adsorbent substances that offer a promising method to quantify and monitor emerging pollutants in complex matrices. MIPs are composed of synthetic materials with pores or cavities that are designed to hold onto a particular target molecule [27]. They have unique characteristics such as specific target recognition, practicability, selectivity, and structural prediction, thereby ensuring a wide range of applications in many fields that include chemical sensing, drug delivery, artificial antibodies, biotechnology, separation science, and water treatment [28]. MIPs are being used in such fields where great selectivity is required, and this includes the specific recognition and separation of biomolecules and contaminants. Their low cost, ease of preparation, reversible adsorption, desorption, and stability make them suitable for the highly selective extraction of various environmental pollutants from aqueous and gaseous samples [29]. For example, Guo et al. [30] and Wang et al. [31] used an intrinsic micropore soluble polymer for the adsorption of organic pollutants from wastewater and the detection of gaseous iodine, respectively.

Malaysia is the second highest exporter of palm oil, cultivating 4.5 million hectares with its agricultural waste amounting to 85.5% (90×106 tons) from the palm oil plantation [32,33]. One such waste is a palm-kernel shell, which is used to produce a carbon-rich material with a solid amorphous structure, nanoporous carbon (NC). The NC has high porosity with so many functional groups containing oxygen, including carboxylic acids, phenols, carbonyls, and lactones, which have garnered significant interest for various ap-

plications in the environmental and energy sector, like the gas and heavy metal adsorption, separation, water treatment, energy storage and supercapacitors, sensors, etc. [34].

Designing a new valuable method with easy implementation and cost effective for the removal of Hg(II) from wastewater remains a challenge. In this work, we show the incorporation of MIP with NC to console the effect of wastewater contamination and palm-kernel shell waste. By keeping in view the advantages of both MIPs and NCs, this present study investigates the Hg(II) adsorption efficacy of MIPs/NC nanocomposite from aqueous samples. For the production of NC from natural sources, a palm-kernel shell was reacted with H_3PO_4 as it served to provide an environmentally friendly, low-cost, and readily available adsorbent. This follows the surface modification of NCs with that of MIP to generate MIPs/NC nanocomposite, which has been tested for the adsorptive removal of Hg(II) from an aqueous solution using the batch method. The formed MIPs/NC nanocomposite has been thoroughly characterized to investigate the morphological, functional groups, surface area, and thermal stability. Further, the tests of efficacy from MIPs/NC nanocomposite proved that the advantages of this work are higher adsorption efficiency and remarkable selection towards Hg(II) ions, as NC materials have shown to be very effective in the field of adsorption and separation due to their tunable textural parameters, thermal and chemical stability. However, the MIPs are known for their highly selective sorbent capacity and are suitable for many bindings with nanosized supports having larger surface areas.

2. Experimental

2.1. Materials

NC from palm-kernel shell (H_3PO_4/500 °C/1 h), L-cysteine (97%), Potassium carbonate (99.9%), 2-Hydroxyethyl methacrylate (99%), and Ethylene glycol dimethacrylate (98%) was used from Sigma-Aldrich. Sodium nitrate (98%) and Methacrylic acid (98%) are from Fluka; [2(methacryloyloxy)ethyl] trimethylammonium chloride (75%) was from Merck; Acetonitrile (99.9) and Benzoyl peroxide (98%) from R&M Chemicals. All chemicals were used directly as received. For solution preparation throughout this study, deionized water was applied.

2.2. Preparation of MIP/NC Nanocomposite

The preparation of MIP/NC nanocomposite involves three steps: complexation of the template to a suitable ligand, polymerization, and removal of the template [27]. Aqueous solution (5%) of potassium carbonate was used to dissolve 5 g of cysteine and 0.2 g of sodium nitrite, respectively. At room temperature, 4 mL of [2(methacryloyloxyethyl)] trimethyl ammonium chloride were slowly administered into the solution and then stirred for 2 h magnetically under nitrogen atmosphere. Afterward, the solution is adjusted to pH 7, thereafter extracted with ethyl acetate. A rotary evaporator is used to evaporate the aqueous phase in which ethanol and ethyl acetate were used to crystallize the residue. Now, 2 mmol cysteine-complex and 0.5 mmol Hg(NO$_3$)$_2$ are then placed in a 50 mL volumetric flask to a total volume of 50 mL with methanol. The mixture was pipetted in a 25 mL beaker bottle, then 0.5 g (6 mmol) methacrylic acid, 0.4 mL (3 mmol) 2-hydroxyethyl methacrylate, 6 mL (30 mmol) ethylene glycol dimethacrylate, and 0.1 g benzoyl peroxide were introduced under nitrogen atmosphere. Following that, each nitrogen-preserved solution received 0.1–0.5 g of NC and 20 mL of acetonitrile (CH$_3$CN) porogens. The solution is then stirred for 30 min before being sealed then purged to nitrogen for 10 min, conveyed to polymerization at 70 °C water bath, which lasted for 3 h. The MIP/NC composites were broken and later crushed with a pestle and mortar into small particles. To remove unreacted monomers, methanol and water solution of (60/40, *v/v*) was used to wash the MIP/NC composites for 24 h. The template was then removed after 48 h at room temperature using thiourea (0.5%) in HCl (0.05 M) solution. The procedure was repeated several times until the mercury analyzer could not detect the template Hg(II) in the filtrate. Finally, the template-free particles were cleaned on a magnetic stirrer with HNO$_3$ (0.1 M) for 3 h to eliminate residual

Hg(II) ions in MIP/NC composites. The same procedure was followed in the synthesis of MIP without adding NC.

2.3. Sample Composite Characterization

Field emission scanning electron microscopy (FESEM; JEOL, JSM7600F, Peabody, MA, USA) was applied to explore the surface morphological feature of the prepared MIP/NC nanocomposite. After overnight drying of the materials at 105 °C and subsequent coating with sputter cutter with a resolution of 5 kV, it provides a direct image of the topographical nature of the surface from all the emitted secondary electrons. Functional groups of the nanocomposite were investigated via infrared spectroscopy (Perkin Elmer, 1650 Spectrometer, Hopkinton, MA, USA). A 0.5 mg powder of the sample was scanned at a resolution of 4 cm^{-1} between 400 and 4000 cm^{-1} wavenumber. A monochromatic light beam with different frequencies is shone on the sample, which absorbs energy from the beam and transmits light of different wavelengths, resulting in the absorption spectrum. The nitrogen adsorption–desorption isotherm in an autosorb analyzer (Quantachrome, Boynton Beach, FL, USA) was used in quantifying the composite surface area, pore volume, and pore size. The BET and BJH equations were employed in evaluating surface area and pore size distribution of the sample material, respectively. Thermal stability of sample material between temperatures ranging from 50 to 800 °C, with a heating rate of 10 °C min^{-1}, and a continuous flow of nitrogen gas at 50 mL min^{-1} was evaluated using TGA (Mettler Toledo 851e, Mettler Toledo, Schwerzenbach, Switzerland).

2.4. Batch Adsorption Set-Up

The metal removal efficacy of the prepared adsorbents was evaluated via batch adsorption experiments. A well-known quantity of the adsorbent was introduced in the 250 mL flasks comprising 100 mg/L of Hg(II) solution. Then, the mixture was shaken at 160 rpm for 2 h at room temperature. At a required interval of time, a certain portion of the mixture was taken to determine the concentration of Hg(II) ions using mercury analyzer (MA—3Solo Mercury Analyzer). The percentage (%) removal and the amount of Hg(II) ions (qt) adsorbed were evaluated via Equations (1) and (2) [35].

$$Removal\ (\%) = \frac{C_0 - C_e}{C_0} \times 100 \tag{1}$$

$$q_t = \frac{(C_0 - C_e)V}{M} \tag{2}$$

C_0 and C_e denote initial concentration and equilibrium concentration (mg/L), V denotes volume of mixture used, and M denotes adsorbent weight (g). The above equations ensured adsorption stability.

2.5. pH Optimization

pH of initial Hg(II) solution for the adsorption was optimized by pH meter and adjusted with NaOH and HCl. The experiment was conducted in a 100 mL solution of Hg(II) with a concentration of 10 mg/L and adsorbent dosage of 0.1 g, with all other parameters held constant.

2.6. Optimization of Adsorbent Dosage

For this, 100 mL solution of Hg(II) metal ion at 10 mg/L concentration, 2 h contact time was used with a pH of 4. Varied adsorbent dosages of 0.1 to 0.5 g. All other parameters remained constant.

2.7. Adsorption Isotherms

Varied concentrations of Hg(II) ions 10, 20, 30, 40, and 50 mg/L in a 100 mL solution at pH 4, and an adsorbent dosage of 0.3 g were used while keeping all other parameters

constant. The two models of Langmuir and Freundlich isotherm were used to describe adsorbent performance properties. The interaction between the equilibrium concentration and adsorbate was investigated using the two adsorption isotherms. On the other hand, the coefficient of separation (RL) was used in determining the adsorption process as favorable, unfavorable, linear, or irreversible [36].

2.8. Adsorption Kinetics

The contact time for Hg(II) ion solution adsorption varied between 15 min, 30 min, 60 min, 90 min, and 120 min. The analysis was performed at pH 4, 25 °C, and with an initial concentration of Hg(II) ion of 30 mg/L. The pseudo-first-order rate equation and pseudo-second-order kinetic model, as shown in Equations (3) and (4), were used to evaluate adsorption kinetics [32].

$$\ln(q_e - q_t) = \ln q_e - k_t \tag{3}$$

where q_e denotes Hg^{2+} adsorption equilibrium (mg/g), q_t is adsorption of Hg(II) at a time t, and k is rate constant that can be determined by plotting $\ln(q_e - q_t)$ versus t (min^{-1}).

$$\frac{t}{q_t} = \frac{1}{k_2 q_e{}^2} + \frac{t}{q_e} \tag{4}$$

where t denotes the amount of Hg(II) ion absorbed at time t (min), and q_t and q_e denote the amount of metal ion adsorbed at respective time t and equilibrium (mg/g). Furthermore, k_2 is the rate constant of second-order adsorption (g/mg min).

2.9. Adsorption Thermodynamics

The thermodynamic study was carried out by immersing Erlenmeyer flasks in a water bath at temperatures ranging from 25 to 50 °C. The experiment was then carried out at pH 4, and the mixture was shaken for 2 h with an initial Hg(II) ions concentration of 30 mg/L. The universal gas constant, R, was used to calculate vital thermodynamic parameters such as enthalpy ΔH, entropy ΔS, and Gibbs free energies ΔG. These findings of the studies were calculated using the following Equations (5) and (6) [37].

$$\Delta G = -RT \ln K_d \tag{5}$$

$$\ln K_d = -\frac{\Delta H}{RT} + \frac{\Delta S}{R} \tag{6}$$

where K_d denotes the adsorption equilibrium constant, R denotes gas constant (KJ/mol·K), and T denotes temperature in Kelvin. Furthermore, slope and intercept of change in enthalpy and entropy were calculated by plotting $\ln K_d$ against $1/T$, respectively.

3. Results and Discussion

3.1. Physicochemical Characterization of MIP/NC Nanocomposite

Table 1 provides the textural properties (nitrogen adsorption–desorption isotherms surface area, pore size, and pore volume) of the NC, MIP, and MIP/NC nanocomposite.

Table 1. Textural properties of NC, MIP, and MIP/NC materials.

Sample	BET Surface Area (m²/g)	Average Pore Volume (cm³/g)	Average Pore Size (nm)
NC	1280	0.677	2.116
MIP	146	0.163	4.468
MIP/NC	884.9	0.389	1.760

The microporosity and surface area in the composite is caused by irregular voids that might be macropores > 50 nm, mesopores 2–50 nm, or even micropores 2 nm in diame-

ter. Figure 1 provides the surface and porosity (average nitrogen adsorption–desorption isotherms) of the MIP (a), NC (b), and MIP/NC (c). Observing the BET area of the MIP without treatment is 146 m^2/g. According to different types of sorption isotherm, Figure 1a is classified as a Type IV adsorption isotherm where this isotherm elucidates the formation of monolayer followed by multilayer. This type shows a hysteresis loop associated with the presence of mesoporosity. With the introduction of NC to generate MIP/NC (Figure 1c), the surface area decreases to 884.9 m^2/g with an average pore volume of 0.389 cm^3/g and an average pore size of 1.760 nm. However, the surface area of MIP/NC is significantly low compared to 1280 m^2/g observed for pure NC (Figure 1b), though both are Type IV with H3 hysteresis loop nitrogen adsorption–desorption isotherms. Further, the micro-porosity was confirmed via the attained distribution of pore size from the BJH technique, as illustrated in Figure 1b. Conversely, the MIP/NC composite retains its appreciable surface area advantageous for heavy metal adsorption, explaining the pores of NC do not completely congest via the MIP's existence.

FTIR spectroscopy provided in Figure 2 confirmed the existence of different functional groups in MIP/NC (a), MIP (b), and NC (c). The comparison of FTIR spectrums for the MIP/NC and MIP composite revealed a characteristic stretching vibration band of hydrogen-bonded alcohol O-H at 3400 cm^{-1} during the polymerization procedure. Furthermore, the broad-band absorption at the high wavenumber region centered at 2987 and 2947 cm^{-1} is determined to belong to the N-H and C-H stretching resulting from a symmetric vibrational bond between carbon, hydrogen, and nitrogen of the MIP/NC composite [38]. The sharp peak that occurred at 1725 cm^{-1} was caused due to vibrational stretching of C=O of the carbonyl group from the cross-linker and monomer as a result of interaction via hydrogen bonding in the synthesis of MIP [25]. However, another vibrational peak appeared at 1634 cm^{-1} assigned to C=O from pure NC (formed from H_3PO_4/1 h/500 °C) [39]. Furthermore, the C-N and C-S stretching vibrations of –NH and –SH groups can be attributed to a sharp peak at the fingerprint region of ~1152 cm^{-1} and responsible for the Hg(II) ions to be corresponding with the non–bonding electron pairs of nitrogen in N–C group [40].
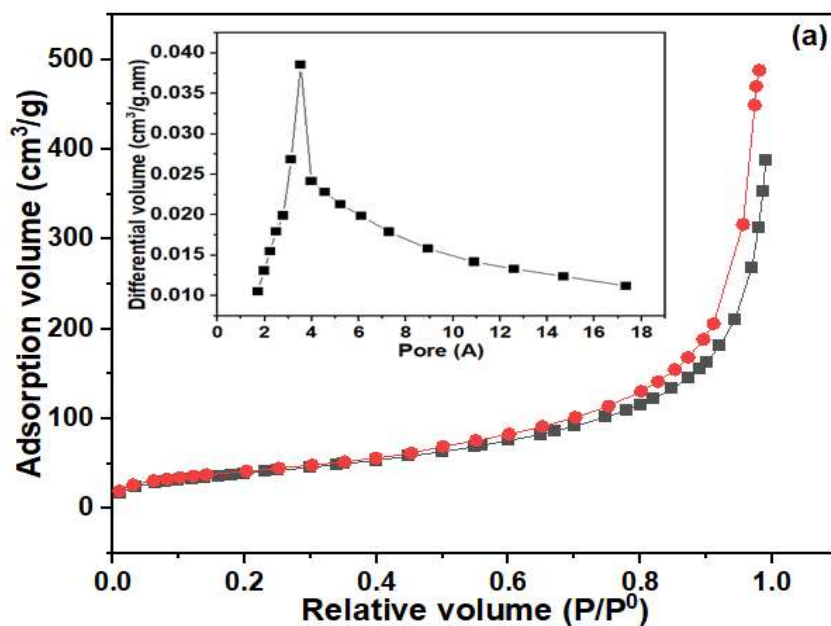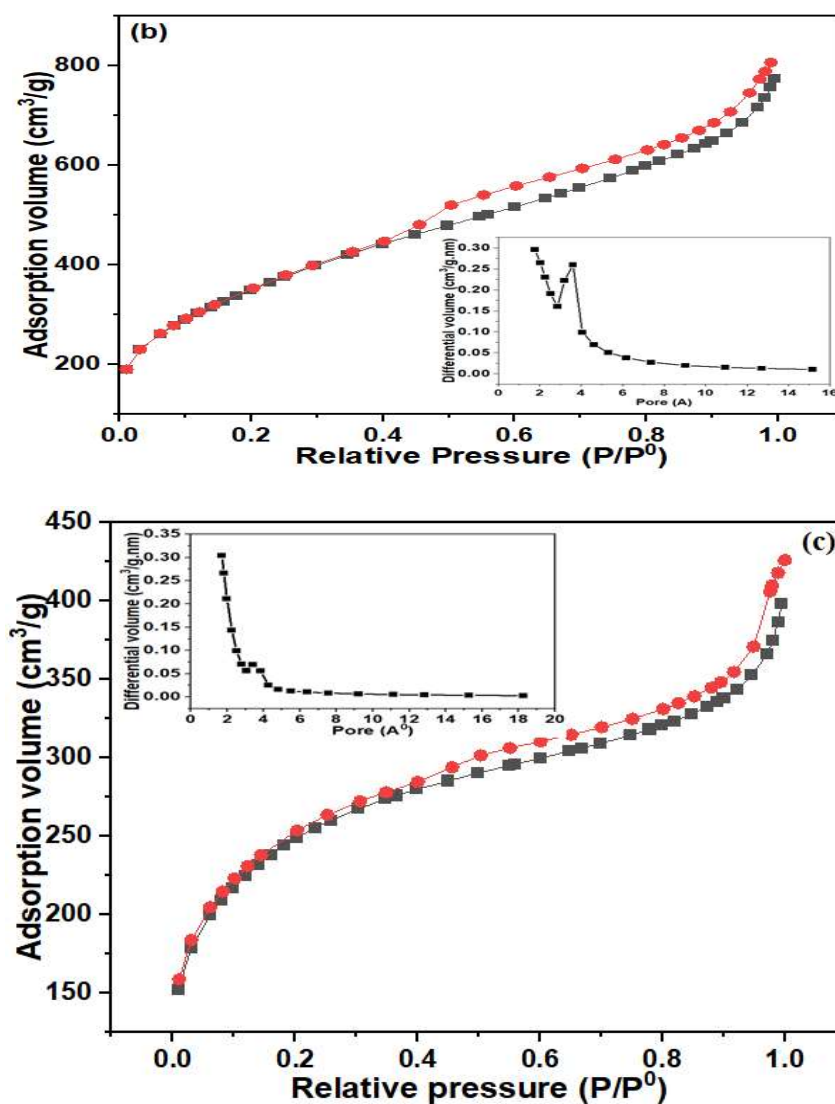

Figure 1. *Cont.*

Figure 1. Isotherms of N_2 adsorption–desorption and pore size distribution of MIP (**a**), NC (**b**), and MIP/NC (**c**). The black and red lines correspond to adsorption and desorption processes respectively.
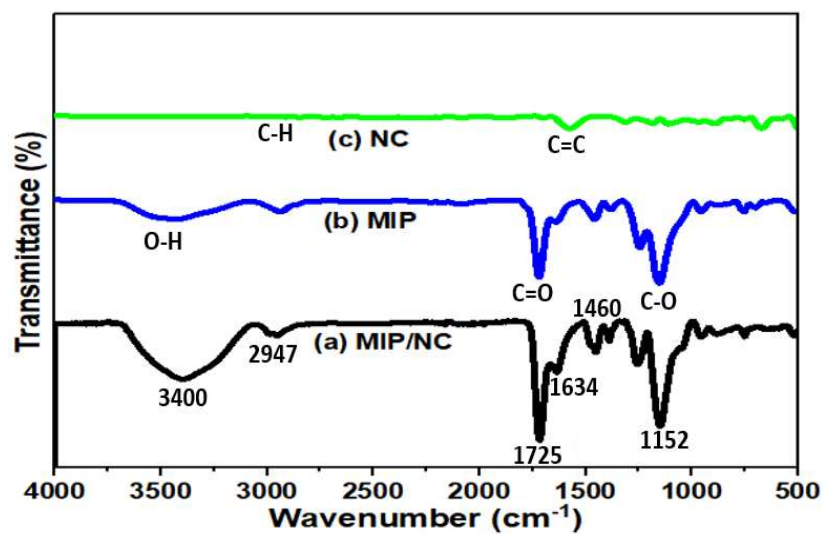

Figure 2. FTIR spectrum of the MIP/NC (a), MIP (b), and NC (c).

Particle morphology (Figure 3), which is described as micro- or macroporous, is an important characterization related to the adsorption efficiency of MIP/NC (a), MIP (b), and NC (c). Figure 3b displayed an electron micrograph of the structural morphology of the MIP with regular pores, spherical shapes, and spots with larger particles crowded with a rough surface. Figure 3c shows a regular smooth surface of pure NC with cracks and crevices, thereby giving a complex of condensed pore structures, larger particles, and surface area displaying the effect of H_3PO_4 evaporation during carbonization. The surface morphology of this study revealed that the chemical treatment of H_3PO_4 is suitable for producing more NC with a large number of cavities and orderly pores that can be occurred at the surface of H_3PO_4-treated carbonized materials [41]. However, MIP/NC nanocomposite (shown in Figure 3a) with a spherical form, irregular, heterogeneous size in which morphology is due to the interaction between the monomer-crosslinker and porogen [42]. This increase in size is caused by particle aggregation and the formation of pores at the surface of MIP/NC during preparation, aiding the fast binding of template molecules [43]. The MIP/NC morphology seems to create an adsorption site or binding and hence enhances the elimination of Hg(II) ions in the mixture.
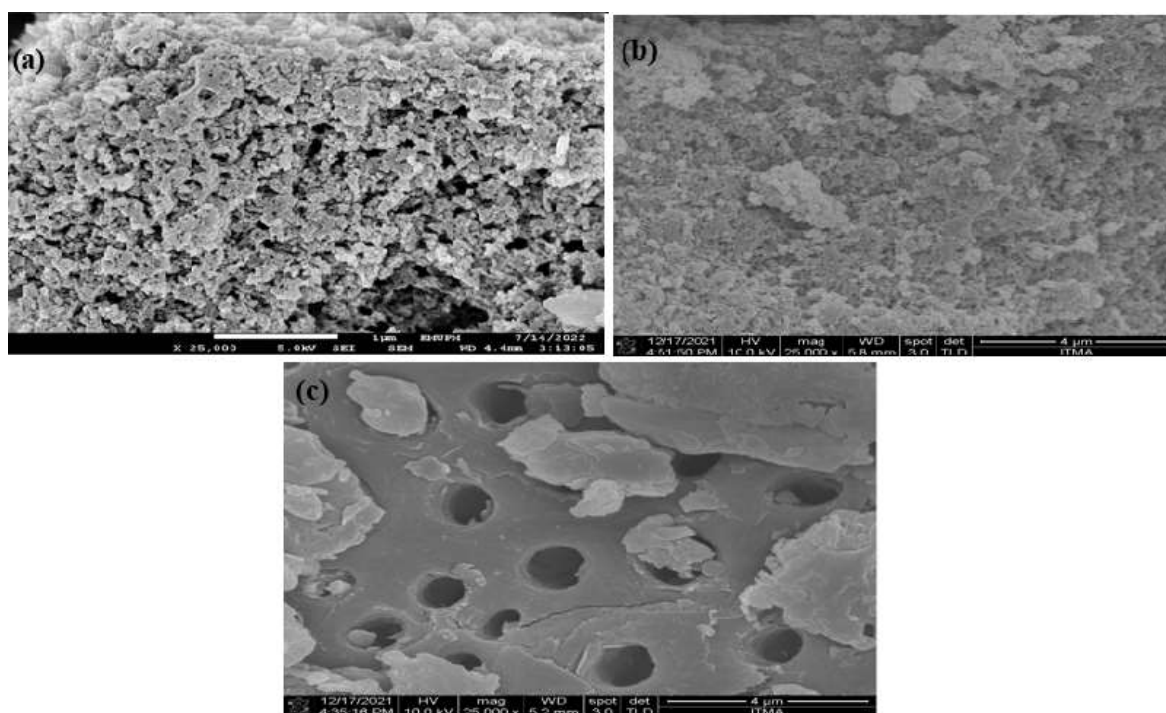

Figure 3. FESEM photographs of MIP/NC (**a**), MIP (**b**), and pure NC (**c**).

Figure 4 represents the thermogram curves of NC, MIP, and MIP/NC nanocomposite analyzed using a TGA analyzer, and the properties measured included material composition and purity, absorbed moisture, and thermal decomposition. In this study, the pure NC material displayed three distinctive peaks of decomposition, which undergoes its first loss of weight before reaching 100 °C. This is ascribed to the absorbed moisture evaporation [44], whereas the second-stage decomposition weight loss occurred around 200–300 °C as a result of hemicellulose and cellulose degradation [45]. The final and last stage of weight loss occurred between 350 and 750 °C due to lignin decomposition [46]. As a result, the H_3PO_4-treated NC is generally stable with more than 50% loss of volatile matter, suggesting the production of a higher thermochemical stable NC.

The MIP/NC nanocomposite TGA results provide a qualitative assessment of the composite, and it is clear that the prepared composite material demonstrated three major stages of decomposition similar to pure NC. With initial decomposition temperatures of MIP/NC below 100 °C, where it exhibited 20.9% weight loss. This is attributed to saturated

water evaporation. The MIP/NC experienced a second weight loss (5.77%) around the temperature of 200–300 °C due to the presence of a cysteine complex that stabilizes the polymer matrix. Also, the final decomposition temperature of MIP/NC ranges between 400 and 450 °C, attributed to the degradation of the lignin complex that stabilizes the polymer matrix. Additionally, the observation of prepared MIP/NC composite's thermal stability up to 400–450 °C affirms it endured extreme environmental situations [47]. In a similar study, the DTG of MIP/NC nanocomposite synthesized from methacrylic acid as a monomer has a decomposition temperature in the range of 270–450 °C by acid group's desiccation, resulting in the formation of anhydrides, which decompose via decarboxylation [48].
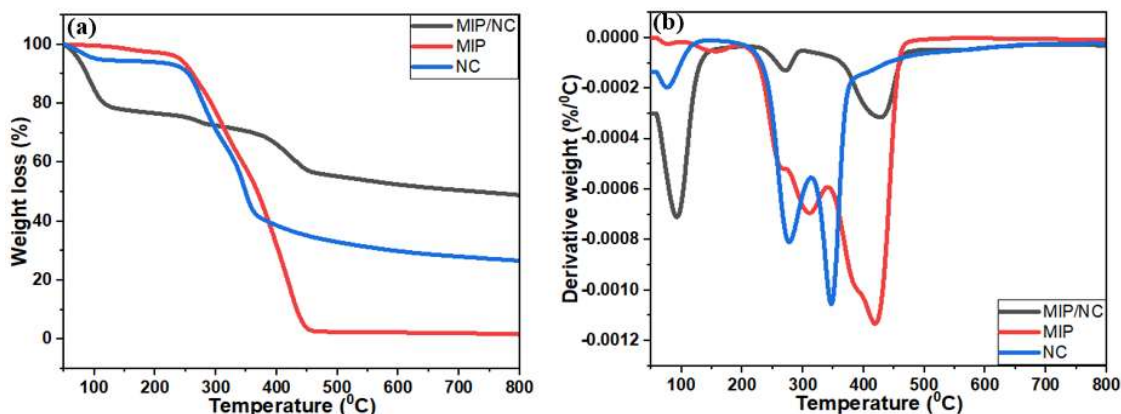

Figure 4. TGA (**a**) and DTG (**b**) thermogram of MIP/NC, MIP, and NC.

3.2. Batch Studies

3.2.1. Effect of pH

The effect of solution pH on carbon-based adsorption performance is obvious because it reflects the concentration level of protolysis in water [49]. The adsorption efficiency of Hg(II) from pH 2 to 6 was applied in evaluating MIP/NC nanocomposite's adsorption efficiency. Figure 5 depicts the increase in solution pH between 2 and 4. The MIP/NC adsorption efficiency increases from 15.5 to 43.7 mg/g. This is because adsorbent surface-active sites can deprotonate and establish a charged surface, signifying that the pH point of zero charge (PZC) for MIP/NC (4.5) is acidic. However, as the pH of the solution rose above 4, there is a decrease in the adsorption capability as a result of metal hydroxide precipitation and its rapid decomposition to oxide, which influences their interaction in the polymer composite [50]. These findings are coherent with Martin-Lara et al., indicating that adsorption efficiency decreased at pH values > 6 [51]. The optimum pH value obtained from the study was pH 4, so pH 4 was found to be suitable for the featured adsorption analysis.
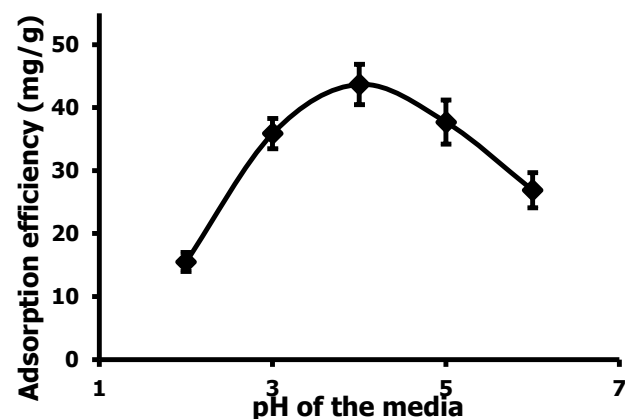

Figure 5. Influence of pH on adsorption efficiency of Hg(II) ion.

3.2.2. Effect of Absorbent Dosage

At optimized pH 4, temperature 25 °C, the dosage of MIP/NC with a varying range of 0.1–0.5 g in 100 mL having 10 mg/L Hg(II) ions. Figure 6 illustrates the impact of adsorption efficiency and % removal of Hg(II) ions on MIP/NC nanocomposite. For 10 mg/L Hg(II), the % removal increased rapidly from 91.3 to 98.4%. The results showed a significant % removal of 97.5% at 0.3 g dosage of MIP/NC. However, above that dosage of MIP/NC, there is no significant improvement in the % removal, although more adsorption sites are available. The absence of Hg(II) molecules in the solution, as well as the presence of an increasing number of active sites free Hg(II) molecule interaction, could explain this. In general, as the adsorbent dosage increases, the % removal also has to be increased due to the an increase in the MIP/NC dosage to ultimately increase the binding spots obtainable for Hg(II) adsorption on the surface as well as the accessibility of exchangeable spots of the Hg(II) ions [36]. However, in our case, the decrease of adsorption efficiency from 49.2 to 24.6 mg/g with an increase of adsorbent dosage from 0.1 to 0.5 g of MIP/NC may have aggregated the composite particles, resulting in a low adsorption capacity. As a result of the accumulation of MIP/NC particles, existing binding spots have decreased, resulting in reduced adsorption efficiency [52].
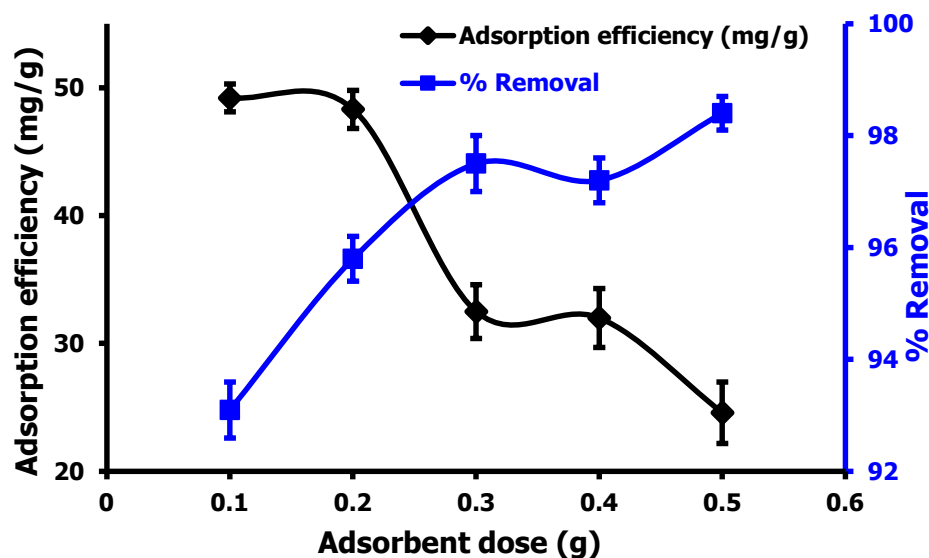

Figure 6. Effect of dosage on Hg(II) ion on adsorption efficiency and % removal of MIP/NC.

3.2.3. Effect of Hg(II) Ion Concentration

The influence of Hg concentration on adsorption efficiency and % removal on MIP/NC was investigated by changing the initial concentration of Hg(II) ions between 10 and 50 mg/L in 100 mL solution. The following were the circumstances, as shown in Figure 7: the adsorbent was 0.3 g in 2 h at a temperature of 25 °C, and the pH was 4 for MIP/NC. From the results, when Hg(II) concentration increases between 10 and 50 mg/L solution, the efficiency of the adsorption increases from 23.4 to 61.3 mg/g. While the Hg(II) solution increased, the binding spots were entirely exploited by the composites, which improved the adsorption efficiency [53]. Roy and Co highlighted that the increases in adsorption efficiency and concentration were due to the decreased resistance to metal ion uptake from solution [54]. However, as the concentration increased from 10 to 50 mg/L, the % removal decreased from 99.5 to 46.7% for the composite. This could be due to the saturation of the ions filling the composites space at critical concentration, causing the % removal to decrease at higher concentrations [55].
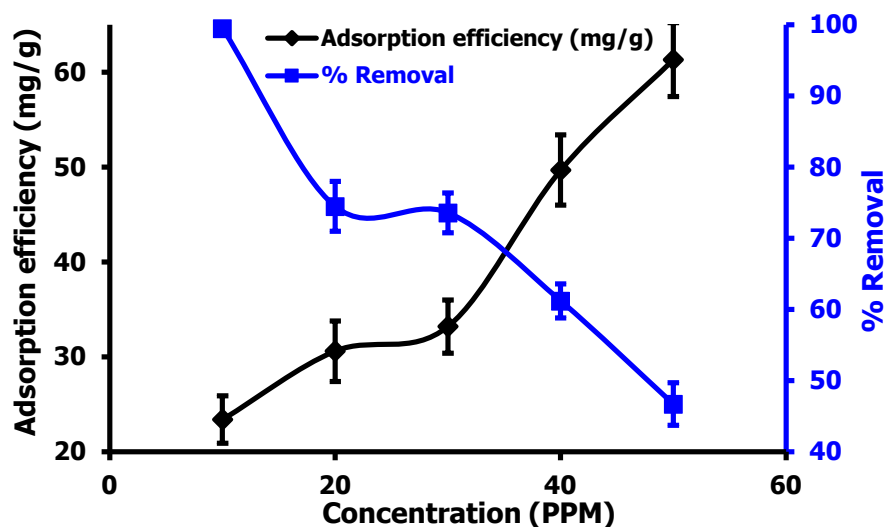
Figure 7. Effect of initial concentration on Hg(II) ion adsorption efficiency and removal percentage of MIP/NC.

3.2.4. Effect of Contact Time

The contact time between the adsorbent and adsorbate is an important parameter in the adsorption process. Figure 8 demonstrates the influence of the contact time of MIP/NC on the uptake efficiency of Hg(II). As shown in the graph, adsorption efficiency improved promptly in the first 1 h due to an increase in the metal ion's adsorption period. However, after 60 min, the increase in adsorption efficiency began to decrease. After 60 min, it was discovered that the increments were negligibly small as the system approached equilibrium [56]. It has been reported that polymeric adsorbent composites have a very fast equilibrium compared to other adsorbents, which can take several days to reach equilibrium [57]. The maximum adsorption efficiency obtained is 49.8 mg/g, and thus, 60 min was chosen as the optimum contact time.
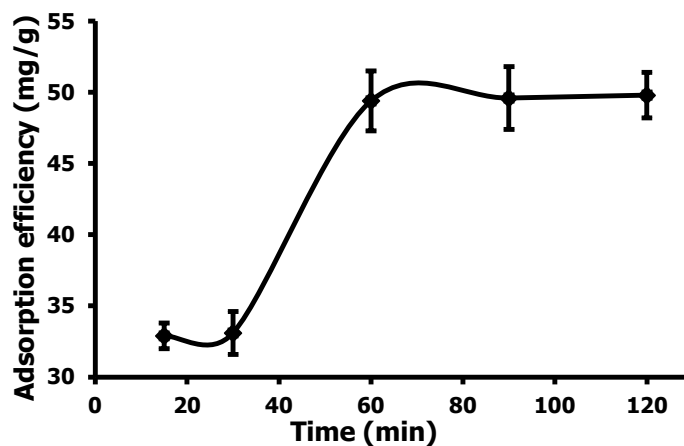

Figure 8. Effect of contact time on Hg(II) ion adsorption efficiency and % removal onto MIP/NC.

3.3. Studies of Hg(II) Adsorption Isotherm

An adsorption isotherm is essential for understanding the uptake mechanism of metal ions and absorbents, where it functions in the solid/liquid phase distribution of molecules as the adsorption reaches an equilibrium where it helps to evaluate the highest uptake efficiency. To measure the uptake mechanisms of MIP/NC, the Langmuir and Freundlich equilibrium adsorption isotherms are employed in describing the interactive behavior of Hg(II) onto the composite. Langmuir's theory adopts the idea that adsorption occurs at a particular homogeneous area of the composite, resulting in monolayer adsorption

capacity. In general, the Freundlich model is more appropriate for illustrating multi-layer adsorption processes on heterogeneous surface adsorbents than the Langmuir isotherm [35]. The following Equations (7) and (8) denote the linear forms of Langmuir and Freundlich isotherms [37].

$$\frac{C_e}{Q_e} = \frac{1}{Q_{max}K_L} + \frac{C_e}{Q_{max}} \tag{7}$$

Q_e denotes the equilibrium concentration of Hg(II) ions (mg/g), K_L denotes the affinity of Hg(II) ions binding to energetic spots composite, and C_e denotes the equilibrium concentration (mg/L). The plot of C_e/Q_e against C_e (Figure 9a) was used to authenticate the Langmuir isotherm, slope, and intercept of the linear-line graph used to calculate the values of Q_{max} and K_L.

$$\log Q_e = \log K_F + \frac{1}{n}\log C_e \tag{8}$$

K_F denotes the intercept demonstrating sorbents uptake efficiency, and $1/n$ is a slope indicating the variation of the adsorption of Hg(II) ions with concentration. The values of K_F and $1/n$ were evaluated using the linear form of the Freundlich kinetic model in a plot of $\log Q_e$ versus $\log C_e$.

Figure 9 displays adsorption fitting for the Langmuir and Freundlich isotherm models of MIP/NC, while Table 2 summarizes the parameters for all adsorption isotherms, constant values, and correlation coefficients for linear fits. The coefficient of correlation (R^2) value closest to 1 determined the best fit of the isotherm models. R^2 values obtained via a linear fitting for Langmuir and Freundlich models in this study were found to be 0.9909 and 0.9965, accordingly. Therefore, the Freundlich model is applicable to the adsorption isotherm model of Hg(II) because its correlation coefficient (R^2) value is greater than the Langmuir correlation coefficient value in the composite (Table 2). This indicates that the Hg(II) uptake happens in multilayers, where an n value greater than 1 specifies a favorable adsorption situation on the composite [42,55]. This conclusion is supported by the kinetic model, which predicts a maximum adsorption capacity for Hg(II) onto MIP/NC of 116 mg/g using the Freundlich isothermal model.

Table 2. Parameters of the Langmuir and Freundlich isotherm model for Hg(II) adsorption via MIP/NC.

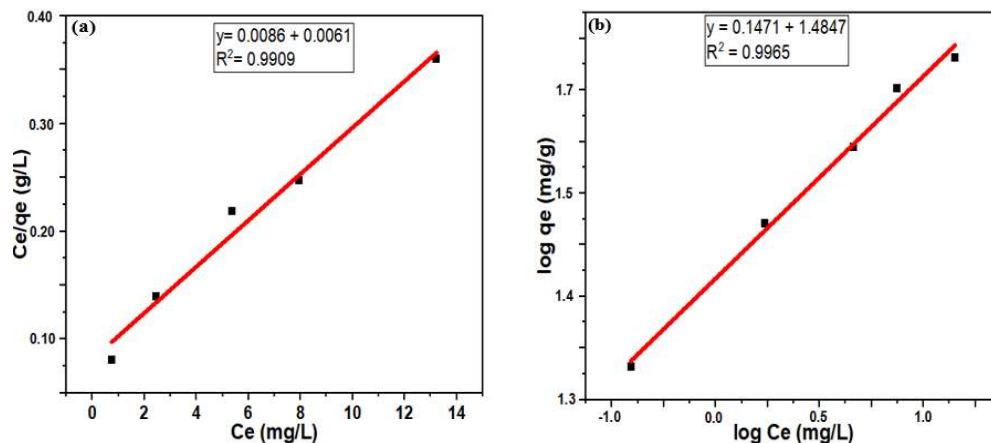| Langmuir Isotherm			Freundlich Isotherm		
Maximum Adsorption Capacity, (mg/g)	Langmuir Constant, K_L (L/mg)	Correlation Coefficient, R^2	Freundlich Constant, K_F (mg/g)	Freundlich Constant, n	Correlation Coefficient, R^2
116	0.708	0.9909	4.03	6.798	0.9965

Figure 9. Langmuir (**a**) and Freundlich (**b**) isotherm models for Hg(II) adsorption on MIP/NC.

3.4. Kinetics of Hg(II) Adsorption

Further investigation of the adsorption behavior of Hg(II) onto MIP/NC nanocomposite in-depth, pseudo-first-order, and pseudo-second-order kinetic models was applied as they determine adsorbents' solute rate activities and provide useful information for researching the adsorption mechanism. Figure 10 illustrates the pseudo-first- and second-order kinetics of Hg(II) adsorption on MIP/NC, where a deficient pseudo-first-order fit to the experimental data provided in Table 3, i.e., a great variance between the experimental and calculated uptake capacity.
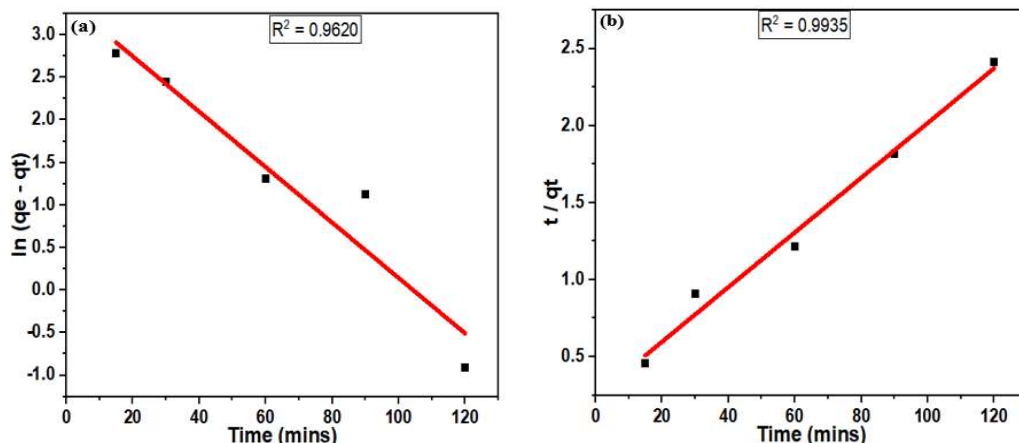

Figure 10. (**a**) Pseudo-first-order and (**b**) pseudo-second-order kinetic models for the adsorption of Hg(II) onto the MIP/NC nanocomposite.

Table 3. Parameters of the pseudo-first- and pseudo-second-order kinetic models for Hg(II) adsorption via MIP/NC nanocomposite.

Kinetic Models	q_e Experimental (mg/g)	q_e Calculated (mg/g)	Correlation Coefficient R^2
Pseudo-first-order	61.34	0.014	0.9620
Pseudo-second-order	61.34	63.60	0.9935

From the table, the correlation coefficient (R^2) value of the pseudo-second-order model of MIP/NC nanocomposite is relatively greater than the pseudo-first-order model. Moreover, the calculated value (q_e, cal) agreed favorably with the experimental q_e value, indicating that the adsorption of Hg(II) onto MIP/NC nanocomposite is following a pseudo-second-order kinetic model. This implies Hg(II) adsorption onto MIP/NC nanocomposite is very fast and is connected to the chemisorption mechanism, which could determine the rate-controlling step [56,58].

3.5. Thermodynamics of Hg(II) Adsorption

The influence of temperature on the uptake efficacy and % removal of Hg(II) onto MIP/NC are presented in Figure 11, where adsorption efficiency and % removal were tested from temperatures of 25, 30, 35, 40, and 50 °C. Figure 11a shows adsorption efficiency and % removal by the MIP/NC nanocomposite slightly decreasing with an increase in temperature, i.e., from 65.5 to 58.7 mg/g and 98.2 to 88.2%, respectively. This could be a result of the weak interaction of Hg(II) and active groups of MIP/NC at higher temperatures, resulting in a weaker bond between the cation and adsorption site, thereby a decrease in adsorption capabilities [59].
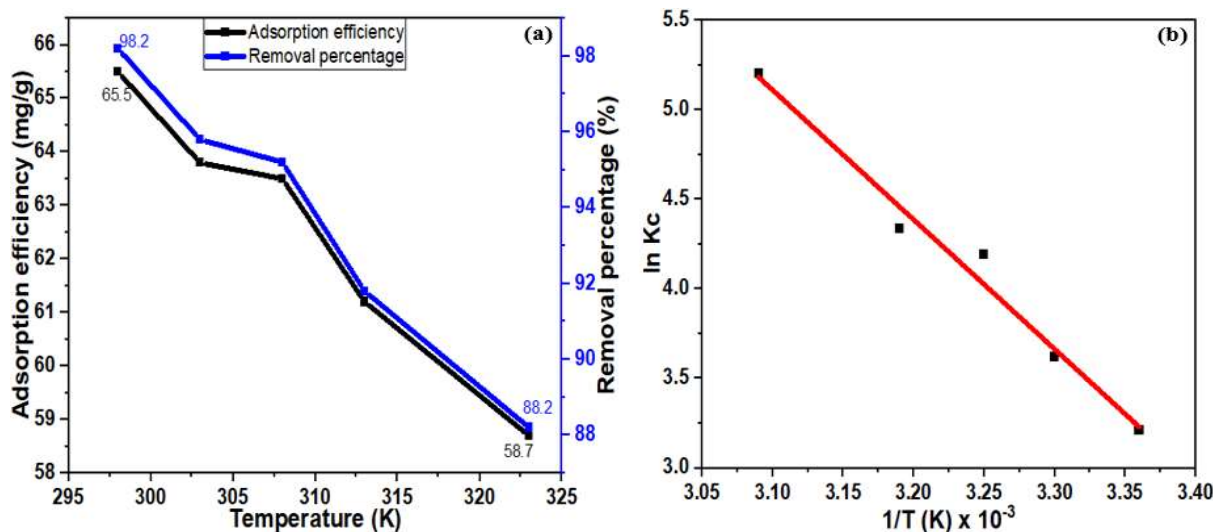
Figure 11. Effect of temperature for Hg(II) adsorption (**a**) and Va not Hoff plot used to calculate the activation energy for Hg(II) adsorption (**b**) on MIP/NC.

Va not Hoff plot in Figure 11b and the data provided in Table 4 were used to estimate the changes in free energy ΔG, enthalpy ΔH, and entropy ΔS related to adsorption of Hg(II) to MIP/NC nanocomposite. These findings had a negative ΔG change and a positive ΔH value, indicating that the adsorption process is endothermic and spontaneous. A positive value of ΔS reflects the increase in randomness at the solid/solution interface during the adsorption of Hg(II) onto the nanocomposite. [35,60].

Table 4. Parameter of thermodynamic studies for Hg(II) adsorption via MIP/NC.

Temperature K	ΔS (KJ/mol K)	ΔH (KJ/mol)	ΔG (KJ/mol)
298			−7.95
303			−9.12
308	34.1	10.55	−10.73
313			−11.28
323			−13.96

3.6. Application of MIP/NC on Condensate Real Sample

The MIP/NC nanocomposite was effectively tested to remove Hg(II) at previously optimized parameters. As a result, a batch method laboratory experiment was carried out on real wastewater of the condensate from the oil and gas industry, with a preliminary concentration of 0.214 mg/L; samples were examined using a mercury analyzer. Adsorption results (not shown here) indicated that the nanocomposite could indeed remove 87.4% Hg(II) wastewater of condensate from the oil and gas industry. It is obvious that synthesized MIP/NC nanocomposite could be used to treat wastewater on a large scale because it is formed from a greener, more maintainable, and less costly adsorbent for removing Hg or its ions from industrial samples.

4. Conclusions

Finally, a MIP/NC nanocomposite with a high BET specific surface area (884.9 m^2/g) was synthesized and tested for the uptake of Hg(II) from aqueous solution via bulk polymerization. The MIP/NC was found to be suitable for the adsorption of Hg(II) under the influence of pH, adsorbent dosage, initial concentration, and contact time in the studies. At pH 4, MIP/NC had a maximum adsorption capacity of 116 mg/g towards Hg(II). However, adsorption isotherm was well integrated into the Freundlich isotherm model, while kinetic studies were based on the pseudo-second-order reaction. Moreover, the

adsorption mechanism is well fitted to spontaneous and endothermic reactions because of its negative free energy and positive enthalpy and entropy values. Furthermore, the prepared composite material was successfully applied in detecting and removing Hg(II) in the real waste condensate from the oil and gas industry. Finally, the synthesized MIP/NC has shown promise as selective adsorbents of Hg(II) in polluted environments, suggesting a variety of combined absorbents of different precursors is recommended to evaluate heavy metal and pharmaceutical removal.

References

1. Awang, N.A.; Wan Salleh, W.N.; Aziz, F.; Yusof, N.; Ismail, A.F. A review on preparation, surface enhancement and adsorption mechanism of biochar-supported nano zero-valent iron adsorbent for hazardous heavy metals. *J. Chem. Technol. Biotechnol.* **2023**, *98*, 22–44. [CrossRef]
2. Schlögl, S.; Diendorfer, P.; Baldermann, A.; Vollprecht, D. Use of industrial residues for heavy metals immobilization in contaminated site remediation: A brief review. *Int. J. Environ. Sci. Technol.* **2023**, *20*, 2313–2326. [CrossRef]
3. Demarco, C.F.; Quadro, M.S.; Selau Carlos, F.; Pieniz, S.; Morselli, L.B.G.A.; Andreazza, R. Bioremediation of Aquatic Environments Contaminated with Heavy Metals: A Review of Mechanisms, Solutions and Perspectives. *Sustainability* **2023**, *15*, 1411. [CrossRef]
4. Chakraborty, R.; Asthana, A.; Singh, A.K.; Jain, B.; Susan, A.B.H. Adsorption of heavy metal ions by various low-cost adsorbents: A review. *Int. J. Environ. Anal. Chem.* **2022**, *102*, 342–379. [CrossRef]
5. Arora, R. Adsorption of heavy metals—A review. *Mater. Today Proc.* **2019**, *18 Pt 7*, 4745–4750. [CrossRef]
6. Da'na, E. Adsorption of heavy metals on functionalized-mesoporous silica: A review. *Microporous Mesoporous Mater.* **2017**, *247*, 145–157. [CrossRef]
7. Economic and Social Commission for Asia and Pacific (ESCAP). SDG 6: Clean Water and Sanitation: Ensure Availability and Sustainable Management of Water and Sanitation for All. 2018. Available online: https://hdl.handle.net/20.500.12870/874 (accessed on 24 May 2023).
8. Arrifano, G.D.P.; Augusto-Oliveira, M.; Lopes-Araújo, A.; Santos-Sacramento, L.; Macchi, B.M.; Nascimento, J.L.M.D.; Crespo-Lopez, M.E. Global Human Threat: The Potential Synergism between Mercury Intoxication and COVID-19. *Int. J. Environ. Res. Public Health* **2023**, *20*, 4207. [CrossRef]
9. Saha, S.; Dhara, K.; Chukwuka, A.V.; Pal, P.; Saha, N.C.; Faggio, C. Sub-lethal acute effects of environmental concentrations of inorganic mercury on hematological and biochemical parameters in walking catfish, Clarias batrachus. *Comp. Biochem. Physiol. Part C Toxicol. Pharmacol.* **2023**, *264*, 109511. [CrossRef]
10. Chen, X.; Hossain, M.F.; Duan, C.; Lu, J.; Tsang, Y.F.; Islam, M.S.; Zhou, Y. Isotherm models for adsorption of heavy metals from water-a review. *Chemosphere* **2022**, *307*, 135545. [CrossRef]
11. Fabre, E.; Lopes, C.B.; Vale, C.; Pereira, E.; Silva, C.M. Valuation of banana peels as an effective biosorbent for mercury removal under low environmental concentrations. *Sci. Total Environ.* **2020**, *709*, 135883. [CrossRef]
12. Kurniawan, T.A.; Lo, W.; Liang, X.; Goh, H.H.; Othman, M.H.D.; Chong, K.K.; Chew, K.W. Remediation technologies for contaminated groundwater due to arsenic (As), mercury (Hg), and/or fluoride (F): A critical review and way forward to contribute to carbon neutrality. *Sep. Purif. Technol.* **2023**, *314*, 123474. [CrossRef]
13. Wu, H.; Lin, G.; Liu, C.; Chu, S.; Mo, C.; Liu, X. Progress and challenges in molecularly imprinted polymers for adsorption of heavy metal ions from wastewater. *Trends Environ. Anal. Chem.* **2022**, *36*, e00178. [CrossRef]
14. Metwally, M.G.; Benhawy, A.H.; Khalifa, R.M.; El Nashar, R.M.; Trojanowicz, M. Application of molecularly imprinted polymers in the analysis of waters and wastewaters. *Molecules* **2021**, *26*, 6515. [CrossRef] [PubMed]

15. Diagboya, P.N.; Olu-Owolabi, B.I.; Adebowale, K.O. Synthesis of covalently bonded graphene oxide–iron magnetic nanoparticles and the kinetics of mercury removal. *Rsc Adv.* **2015**, *5*, 2536–2542. [CrossRef]

16. Huang, R.; Ma, X.; Li, X.; Guo, L.; Xie, X.; Zhang, M.; Li, J. A novel ion-imprinted polymer based on graphene oxide-mesoporous silica nanosheet for fast and efficient removal of chromium (VI) from aqueous solution. *J. Colloid Interface Sci.* **2018**, *514*, 544–553. [CrossRef] [PubMed]

17. Lyu, Q.; Liu, Y.; Guan, Y.; Liu, X.; Che, D. DFT study on the mechanisms of mercury removal from natural gas over Se-modified activated carbon. *Fuel* **2022**, *324*, 124658. [CrossRef]

18. Egirani, D.; Latif, M.T.; Wessey, N.; Poyi, N.R.; Shehata, N. Preparation and characterization of powdered and granular activated carbon from Palmae biomass for mercury removal. *Appl. Water Sci.* **2021**, *11*, 10. [CrossRef]

19. Rodriguez, R.; Contrino, D.; Mazyck, D.W. Role of activated carbon precursor in mercury removal. *Ind. Eng. Chem. Res.* **2020**, *59*, 17740–17747. [CrossRef]

20. Gai, K.; Avellan, A.; Hoelen, T.P.; Lopez-Linares, F.; Hatakeyama, E.S.; Lowry, G.V. Impact of mercury speciation on its removal from water by activated carbon and organoclay. *Water Res.* **2019**, *157*, 600–609. [CrossRef]

21. Abdullah, N.S.; Sharifuddin, S.S.; Hussin, M.H. Study on adsorption of mercury from aqueous solution on activated carbons prepared from palm kernel shell. *Key Eng. Mater.* **2018**, *783*, 109–114. [CrossRef]

22. Hadavifar, M.; Bahramifar, N.; Younesi, H.; Li, Q. Adsorption of mercury ions from synthetic and real wastewater aqueous solution by functionalized multi-walled carbon nanotube with both amino and thiolated groups. *Chem. Eng. J.* **2014**, *237*, 217–228. [CrossRef]

23. Jeon, C.; Solis, K.L.; An, H.R.; Hong, Y.; Igalavithana, A.D.; Ok, Y.S. Sustainable removal of Hg (II) by sulfur-modified pine-needle biochar. *J. Hazard. Mater.* **2020**, *388*, 122048. [CrossRef] [PubMed]

24. Bailon, M.X.; Chaudhary, D.K.; Jeon, C.; Ok, Y.S.; Hong, Y. Impact of sulfur-impregnated biochar amendment on microbial communities and mercury methylation in contaminated sediment. *J. Hazard. Mater.* **2022**, *438*, 129464. [CrossRef]

25. Zhang, Y.; Yan, L.; Xu, W.; Guo, X.; Cui, L.; Gao, L.; Du, B. Adsorption of Pb (II) and Hg (II) from aqueous solution using magnetic $CoFe_2O_4$-reduced graphene oxide. *J. Mol. Liq.* **2014**, *191*, 177–182. [CrossRef]

26. Du, W.; Yin, L.; Zhuo, Y.; Xu, Q.; Zhang, L.; Chen, C. Catalytic oxidation and adsorption of elemental mercury over $CuCl_2$-impregnated sorbents. *Ind. Eng. Chem. Res.* **2014**, *53*, 582–591. [CrossRef]

27. Rahim, Z.A.; Yusof, N.A.; Ismail, S.; Mohammad, F.; Abdullah, J.; Rahman, N.A.; Abubakar, L.; Soleiman, A.A. Functional nano molecularly imprinted polymer for the detection of Penicillin G in pharmaceutical samples. *J. Polym. Res.* **2023**, *30*, 113. [CrossRef]

28. Bagheri, A.R.; Aramesh, N.; Khan, A.A.; Gul, I.; Ghotekar, S.; Bilal, M. Molecularly imprinted polymers-based adsorption and photocatalytic approaches for mitigation of environmentally-hazardous pollutants—A review. *J. Environ. Chem. Eng.* **2021**, *9*, 104879. [CrossRef]

29. Villarreal-Lucio, D.S.; Vargas-Berrones, K.X.; Díaz de León-Martínez, L.; Flores-Ramíez, R. Molecularly imprinted polymers for environmental adsorption applications. *Environ. Sci. Pollut. Res.* **2022**, *29*, 89923–89942. [CrossRef]

30. Guo, H.; Li, H.; Jing, C.; Wang, X. Soluble polymers with intrinsic porosity for efficient removal of phenolic compounds from water. *Microporous Mesoporous Mater.* **2021**, *319*, 111068. [CrossRef]

31. Wang, X.; Yu, C.; Guo, H.; Cheng, Y.; Li, Y.; Zheng, D.; Feng, S.; Lin, Y. Robust fluorescent detection of iodine vapor by a film sensor based on a polymer of intrinsic microporosity. *Chem. Eng. J.* **2022**, *438*, 135641. [CrossRef]

32. Baby, R.; Hussein, M.Z.; Zainal, Z.; Abdullah, A.H. Preparation of Functionalized Palm Kernel Shell Bio-adsorbent for the treatment of heavy metal-contaminated water. *J. Hazard. Mater. Adv.* **2023**, *10*, 100253. [CrossRef]

33. Uchegbulam, I.; Momoh, E.O.; Agan, S.A. Potentials of Palm Kernel Shell Derivatives: A Critical Review on Waste Recovery for Environmental Sustainability. *Clean. Mater.* **2022**, *6*, 100154. [CrossRef]

34. Singh, G.; Lee, J.M.; Kothandam, G.; Palanisami, T.; Al-Muhtaseb, A.A.H.; Karakoti, A.; Vinu, A. A review on the synthesis and applications of nanoporous carbons for the removal of complex chemical contaminants. *Bull. Chem. Soc. Jpn.* **2021**, *94*, 1232–1257. [CrossRef]

35. Aliyu, M.; Abdullah, A.H.; bin Mohamed Tahir, M.I. Adsorption tetracycline from aqueous solution using a novel polymeric adsorbent derived from the rubber waste. *J. Taiwan Inst. Chem. Eng.* **2022**, *136*, 104333. [CrossRef]

36. Jena, K.K.; Reddy, K.S.K.; Karanikolos, G.N.; Choi, D.S. L-Cysteine and silver nitrate based metal sulfide and Zeolite-Y nano adsorbent for efficient removal of mercury (II) ion from wastewater. *Appl. Surf. Sci.* **2023**, *611*, 155777. [CrossRef]

37. Aliyu, M.; Abdullah, A.H.; bin Mohamed Tahir, M.I. A Potential Approach for Converting Rubber Waste into a Low-Cost Polymeric Adsorbent for Removing Methylene Blue from Aqueous Solutions. *Indones. J. Chem.* **2022**, *22*, 653–665. [CrossRef]

38. Samah, N.A.; Rosli, N.A.M.; Manap, A.H.A.; Aziz, Y.F.A.; Yusoff, M.M. Synthesis & characterization of ion imprinted polymer for arsenic removal from water: A value addition to the groundwater resources. *Chem. Eng. J.* **2020**, *394*, 124900. [CrossRef]

39. Yeboah, M.L. Facile synthesis of micro-mesoporous activated carbon in ambient air via one and two-stage activation of palm kernel shell waste for methylene blue adsorption. *Int. J. Environ. Anal. Chem.* **2021**, 1–19. [CrossRef]

40. Roushani, M.; Abbasi, S.; Khani, H. Synthesis and application of ion-imprinted polymer nanoparticles for the extraction and preconcentration of mercury in water and food samples employing cold vapor atomic absorption spectrometry. *Environ. Monit. Assess.* **2015**, *173*, 266–273. [CrossRef]

41. Lee, J.; Kim, S.; Shin, H. Hierarchical porous carbon electrodes with sponge-like edge structures for the sensitive electrochemical detection of heavy metals. *Sensors* **2021**, *21*, 1346. [CrossRef]

42. Meléndez-Marmolejo, J.; Díaz de León-Martínez, L.; Galván-Romero, V.; Villarreal-Lucio, S.; Ocampo-Pérez, R.; Medellín-Castillo, N.A.; Flores-Ramírez, R. Design and application of molecularly imprinted polymers for adsorption and environmental assessment of anti-inflammatory drugs in wastewater samples. *Environ. Sci. Pollut. Res.* **2022**, *29*, 45885–45902. [CrossRef]

43. Ensafi, A.A.; Nasr-Esfahani, P.; Rezaei, B. Synthesis of molecularly imprinted polymer on carbon quantum dots as an optical sensor for selective fluorescent determination of promethazine hydrochloride. *Sens. Actuators B Chem.* **2018**, *257*, 889–896. [CrossRef]

44. Elaigwu, S.E.; Greenway, G.M. Characterization of energy-rich hydrochars from microwave-assisted hydrothermal carbonization of coconut shell. *Waste Biomass Valorization* **2019**, *10*, 1979–1987. [CrossRef]

45. Nasir, S.; Hussein, M.Z.; Zainal, Z.; Yusof, N.A.; Mohd Zobir, S.A. Electrochemical energy storage potentials of waste biomass: Oil palm leaf-and palm kernel shell-derived activated carbons. *Energies* **2018**, *11*, 3410. [CrossRef]

46. Li, Y.; Zhang, X.; Yang, R.; Li, G.; Hu, C. The role of H_3PO_4 in the preparation of activated carbon from NaOH-treated rice husk residue. *RSC Adv.* **2015**, *5*, 32626–32636. [CrossRef]

47. Saleh, T.A.; Sarı, A.; Tuzen, M. Optimization of parameters with experimental design for the adsorption of mercury using polyethylenimine modified-activated carbon. *J. Environ. Chem. Eng.* **2017**, *5*, 1079–1088. [CrossRef]

48. Dima, S.O.; Sarbu, A.; Dobre, T.; Purcar, V.; Nicolae, C.A. Diosgenin selective molecularly imprinted polymers with acrylonitrile-methacrylic acid matrix. *Mater. Plast.* **2012**, *49*, 106–113. [CrossRef]

49. Duan, C.; Ma, T.; Wang, J.; Zhou, Y. Removal of heavy metals from aqueous solution using carbon-based adsorbents: A review. *J. Water Process Eng.* **2020**, *37*, 101339. [CrossRef]

50. Wu, G.; Wang, Z.; Wang, J.; He, C. Hierarchically imprinted organic–inorganic hybrid sorbent for selective separation of mercury ion from aqueous solution. *Anal. Chim. Acta* **2007**, *582*, 304–310. [CrossRef]

51. Martín-Lara, M.A.; Calero, M.; Ronda, A.; Iáñez-Rodríguez, I.; Escudero, C. Adsorptive behavior of an activated carbon for bisphenol A removal in single and binary (bisphenol A—Heavy metal) solutions. *Water* **2020**, *12*, 2150. [CrossRef]

52. Shafqat, S.R.; Bhawani, S.A.; Bakhtiar, S.; Ibrahim, M.N.M. Synthesis of molecularly imprinted polymer for removal of Congo red. *BMC Chem.* **2020**, *14*, 27. [CrossRef] [PubMed]

53. Liu, Z.; Sun, Y.; Xu, X.; Qu, J.; Qu, B. Adsorption of Hg (II) in an aqueous solution by activated carbon prepared from rice husk using KOH activation. *ACS Omega* **2020**, *5*, 29231–29242. [CrossRef] [PubMed]

54. Roy, P.; Dey, U.; Chattoraj, S.; Mukhopadhyay, D.; Mondal, N.K. Modeling of the adsorptive removal of arsenic (III) using plant biomass: A bioremedial approach. *Appl. Water Sci.* **2017**, *7*, 1307–1321. [CrossRef]

55. Gheitasi, F.; Ghammamy, S.; Zendehdel, M.; Semiromi, F.B. Removal of mercury (II) from aqueous solution by powdered activated carbon nanoparticles prepared from beer barley husk modified with Thiol/Fe_3O_4. *J. Mol. Struct.* **2022**, *1267*, 133555. [CrossRef]

56. Chen, J.; Tan, L.; Cui, Z.; Qu, K.; Wang, J. Graphene oxide molecularly imprinted polymers as novel adsorbents for solid-phase microextraction for selective determination of norfloxacin in the marine environment. *Polymers* **2022**, *14*, 1839. [CrossRef] [PubMed]

57. Bashir, K.; Guo, P.; Chen, G.; Li, Y.; Ge, Y.; Shu, H.; Fu, Q. Synthesis, characterization, and application of griseofulvin surface molecularly imprinted polymers as the selective solid phase extraction sorbent in rat plasma samples. *Arab. J. Chem.* **2020**, *13*, 4082–4091. [CrossRef]

58. Han, X.; Zhang, X.; Zhong, L.; Yu, X.; Zhai, H. Preparation of sulfamethoxazole molecularly imprinted polymers based on magnetic metal–organic frameworks/graphene oxide composites for the selective extraction of sulfonamides in food samples. *Microchem. J.* **2022**, *177*, 107259. [CrossRef]

59. Li, B.; Xiong, H.; Xiao, Y. Progress on synthesis and applications of porous carbon materials. *Int. J. Electrochem. Sci* **2020**, *15*, 1363–1377. [CrossRef]

60. Wieszczycka, K.; Filipowiak, K.; Wojciechowska, I.; Aksamitowski, P. Novel ionic liquid-modified polymers for highly effective adsorption of heavy metals ions. *Sep. Purif. Technol.* **2020**, *236*, 116313. [CrossRef]